Seasonality in Site Response: An Example from Two Historical Earthquakes in Kazakhstan

Rami Alshembari[1], Stefano Parolai[2], Tobias Boxberger[3], Denis Sandron[*2], Marco Pilz[3], and Natalya Sylacheva[4]

Abstract

During the past 150 yr, the city of Almaty (formerly Verny) in Kazakhstan has suffered significant damage due to several large earthquakes. The 9 June 1887 M_w 7.3 Verny earthquake occurred at a time when the city mainly consisted of adobe buildings with a population of 30,000, with it being nearly totally destroyed with 300 deaths. The 3 January 1911 M_w 7.8 Kemin earthquake caused 390 deaths, with 44 in Verny itself. Remarkably, this earthquake, which occurred around 40 km from Verny, caused significant soil deformation and ground failure in the city. A crucial step toward preparing for future events, mitigating against earthquake risk, and defining optimal engineering designs, involves undertaking site response studies. With regard to this, we investigate the possibility that the extreme ground failure observed after the 1911 Kemin earthquake could have been enhanced by the presence of a shallow frozen ground layer that may have inhibited the drainage of pore pressure excess through the surface, therefore inducing liquefaction at depth. We make use of information collected regarding the soil conditions around the city at the time of the earthquakes, the results from seismic noise analysis, borehole data, and surface temperature data. From these datasets, we estimated the necessary parameters for evaluating the dynamic properties of the soil in this area. We successively characterize the corresponding sediment layers at the sites of the observed liquefaction. Although the estimated soil parameters are not optimally constrained, the dynamic analysis, carried out using selected strong-motion recordings that are expected to be compatible with the two considered events, indicated that the extensive ground failure that occurred during the Kemin event could be due to the presence of a superficial frozen soil layer. Our results indicate that for this region, possible seasonal effects should, therefore, be considered when undertaking site effect studies.

Introduction

The city of Almaty (Fig. 1), formerly known as Verny, is the largest city in Kazakhstan, with around 1.85 million inhabitants, and was the country's capital until 1997. During the past two centuries, Almaty has suffered significant damage due to several large earthquakes (Silacheva *et al.*, 2014; Kulikova and Krüger, 2015; Krüger *et al.*, 2017; Mosca *et al.*, 2019). In particular, the 1887 M_w 7.3 Verny earthquake (Arrowsmith *et al.*, 2017) struck the newly built town. At that time, the town mainly consisted of adobe buildings with a population of around 30,000. As a result of this event, the town was nearly totally destroyed, with a death toll of nearly 300.

Another damaging event was the 1911 M_w 7.8 Kemin earthquake (Bindi *et al.*, 2014), and, from the reports of that time, all buildings suffered some degree of damage (Bogdanovic, 1911; Bogdanovich *et al.*, 1914). Because of this earthquake, 390 people died, 44 of them in Verny itself. Remarkably, this earthquake generated in Verny (nearly 40 km from the epicenter) large amounts of soil deformation and ground failure, in particular in the loam sandy soils. Cracks in some places reached 1 m in width and 5 m in depth (Fig. 2).

While the Verny earthquake struck the city at the end of spring (9 June), the Kemin event happened in the middle of the winter season (3 January). The ground in Almaty, due to the average air temperature during that period with values significantly below zero (Razuvaev *et al.*, 2008), is expected to have

1. International Centre for Theoretical Physics, Trieste, Italy; 2. Istituto Nazionale di Oceanografia e di Geofisica Sperimentale, Sgonico (TS), Italy; 3. Helmholtz-Zentrum Potsdam, German Research Center for Geosciences, Potsdam, Germany; 4. Limited Liability Company, Institute of Seismology, Almaty, Kazakhstan

*Corresponding author: dsandron@inogs.it

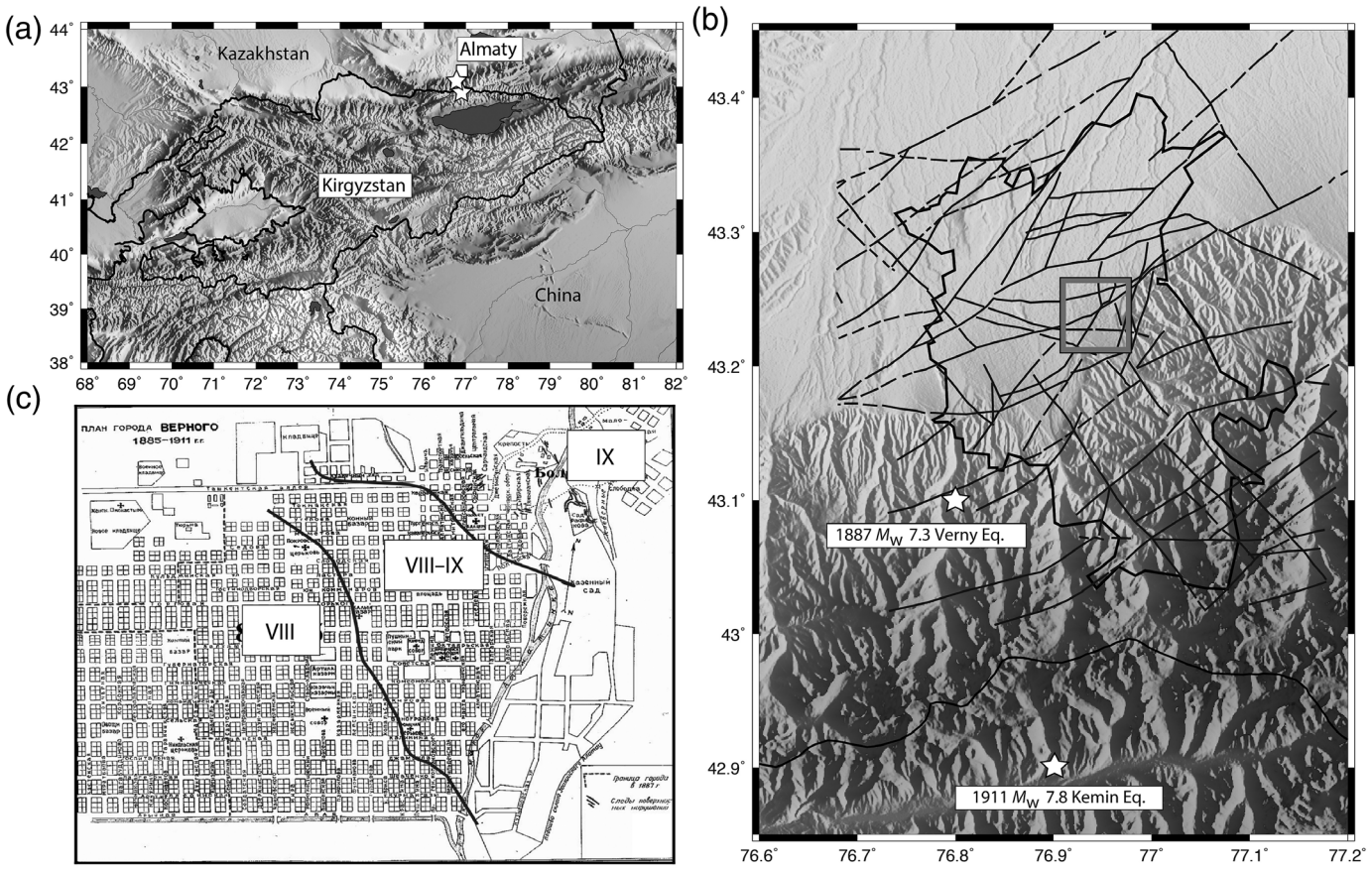

Figure 1. (a) Almaty (formerly Verny), southern Kazakhstan. The white stars indicate the epicenters of the two large earthquakes considered in this study: the 9 June 1887 M_W 7.3 Verny and the 3 January 1911 M_W 7.8 Kemin events. (b) Present urban area of Almaty and the position of the epicenters. The ancient urban settlement of Verny is marked by the gray box. The known active faults are shown as thin black lines. (c) Distribution of macroseismic intensity in the Verny area due to the Kemin event (redrawn after Nurmagambetov *et al.*, 1999). The black lines indicate the areas where liquefaction and ground failures occurred.

been frozen in the uppermost meter, which might have led to a different ground response to the incoming seismic waves.

It is worth remembering that a key step for seismic hazard assessment and risk mitigation is the estimation of the ground motion that earthquakes can generate at a given site. This estimate must also include possible local effects due to the propagation of waves in the shallower geological layers. For small-to-moderate earthquake shaking, the soil can be expected to respond linearly to ground-motion excitation, and simple site response analysis, based on empirical data or numerical simulations, are sufficient to provide an overview of the possible spatial variation of ground motion. However, when the level of shaking increases, soft soil material starts behaving nonlinearly and, in particular cases, liquefaction phenomena and ground failure might occur (Kramer, 1996).

Within several initiatives aiming at seismic risk assessment and mitigation in Central Asia (e.g., the Earthquake Model Central Asia [EMCA] project, see Data and Resources), the site response in Almaty was estimated by means of earthquake and noise recordings (Pilz *et al.*, 2015). In addition, three array measurements of ambient seismic noise were carried out to extract shear-wave velocity profiles, an essential parameter for evaluating the dynamic properties of soil, and to characterize the corresponding sediment layers at each site. These data together with those derived by previous investigations (Silacheva *et al.*, 2014) allow the identification of areas with different site responses. However, these kinds of analyses are not sufficient for answering the question of why the Kemin earthquake cause a different response compared to the Verny event (in particular, a much greater occurrence of liquefaction and ground failure). The first reason for explaining the differences might be the different levels of ground shaking induced by each earthquake. However, Figure 3 shows that when considering the estimated epicenter positions of the two events and their corresponding magnitudes, the level of shaking induced in Almaty, at least in terms of peak ground acceleration (PGA), is similar. The level of shaking was calculated using the ground-motion prediction equation (GMPE) proposed by Boore and Atkinson (2008) as suggested for intraplate areas by the Global Earthquake Model (GEM) (Ullah, 2016).

Figure 2. Ground failure effects documented after the 3 January 1911 Kemin earthquake (modified from Nurmagambetov *et al.*, 1999).

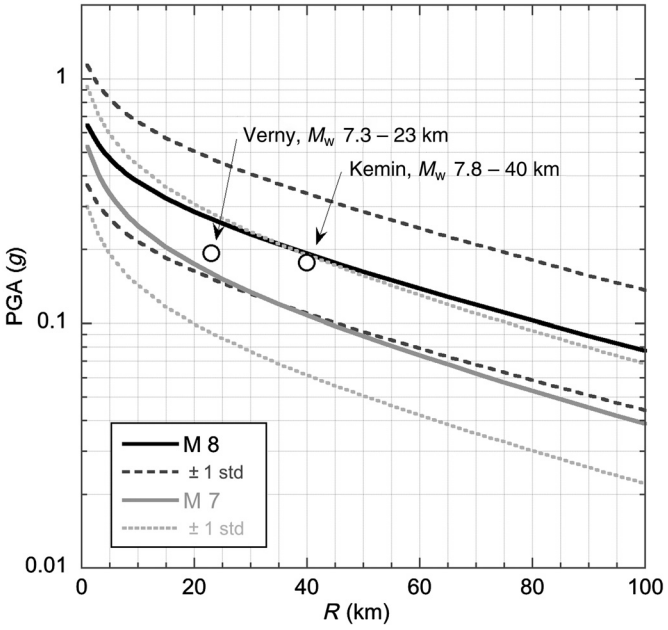

Figure 3. Estimated peak ground acceleration (PGA) for the 1887 M_w 7.3 Verny and the 1911 M_w 7.8 Kemin earthquakes (Bindi *et al.*, 2014) using the ground-motion prediction equation (GMPE) proposed by Boore and Atkinson (2008), as suggested for intraplate areas by the Global Earthquake Model (GEM). *R* is the closest horizontal distance to the earthquakes' epicenters.

Because major differences in the level of shaking can be ruled out as being responsible for the different ground failure caused by the two earthquakes, we therefore formulate and verify the hypothesis that the strong liquefaction and ground failure during the Kemin earthquake was caused by the presence of a frozen superficial soil layer. This layer, by preventing drainage through the surface, did not allow the excess pore water pressure to dissipate.

The analysis we propose is similar to that carried out by Finn *et al.* (1978) to explain the occurrence of liquefaction during the 1964 M_w 9.2 Alaska earthquake. The recent 30 November 2018 Alaska earthquake dramatically provided new evidence of such effects. In the case considered in this study, we are not concentrating on the modification of the ground motion due to the frozen layer as in Vinson (1978), Wang *et al.* (2004), and Xu *et al.* (2011), but rather we mainly focus on its influence on the pore pressure increase as a result of the seasonal conditions. Unfortunately, because the amount of information available about the soil conditions in Almaty is still limited (in terms of geotechnical data), to verify if the proposed hypothesis could be feasible, we explore several different possible soil structure models.

The models were derived after analyzing the available parameters that allow the evaluation of the dynamic properties of soil. Then, we selected a strong-motion recording according to the expected source characteristics (considering the regional tectonics and information available from the literature) and epicentral position with respect the target site. The recording was matched to predefined response spectra using a suitable GMPE to be compatible with the 1911 Kemin and 1887 Verny earthquakes. The resulting time series were used as input for the dynamic analysis.

Data Availability and Models

To study the *S*-wave velocity structure with depth, seismic noise microarray measurements were carried out in Almaty. In summer 2014, one array was installed in the northern part of the city, close to the location of the Verny urban area at the beginning of the twentieth century (gray box in Fig. 1b).

Array measurements were carried out using 16 broadband receivers and for durations of not less than 120 min. Seismic noise data were divided into windows of 120 s, and the

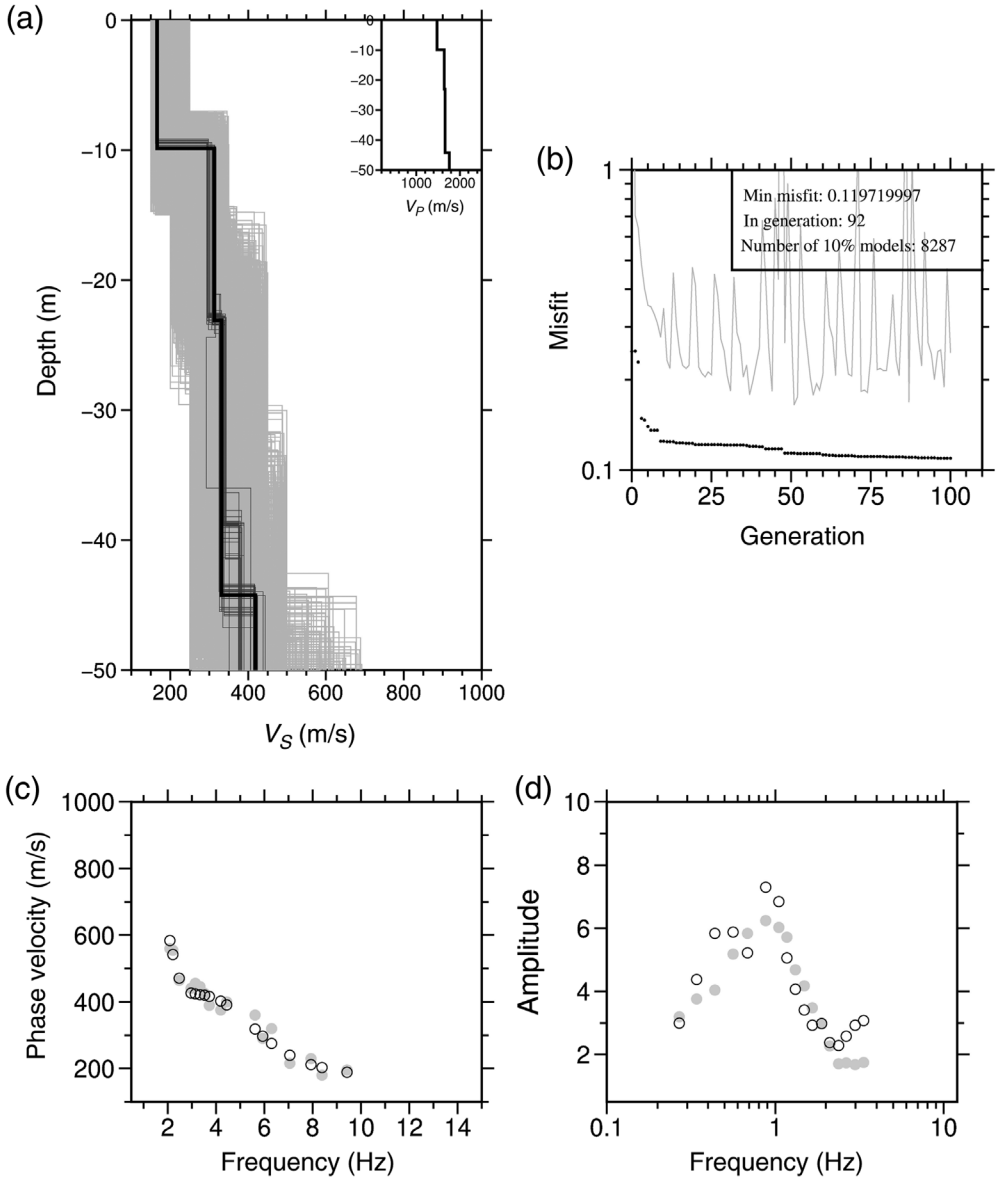

Figure 4. Shear-wave velocity profiles for array measurement sites in Almaty (see Fig. 1b, the grey box). (a) Tested *S*-wave velocity models (inset refers to *P* wave) from the considered genetic algorithm (gray lines) and the best-fitting model (black line). (b) Minimum misfit (black dots) and the average misfit (gray line) at each generation. (c) Observed phase velocities (filled gray circles) and the calculated one for the best-fitting model (black circles). (d) Observed horizontal-to-vertical (H/V) ratio (filled gray circles) and the calculated one for the best-fitting model (black circles).

extended spatial autocorrelation method was applied (Ohori *et al.*, 2002; Parolai *et al.*, 2005). The estimated Rayleigh-wave dispersion curves were inverted jointly with the horizontal-to-vertical (H/V) curves following the scheme proposed by Parolai *et al.* (2005). The results indicated that the *S*-wave velocity in the uppermost 10 m is equal to 167 m/s, while it increases to 320 m/s over the next 20 m (Fig. 4). Although the minimum misfit is not changing significantly after 75 iterations, the average one shows large variations since the algorithm is trying to explore different part of the solution space. The depth of 30 m was assumed to be the input depth of the ground motion in the numerical simulations, considering that liquefaction is expected to occur mainly in the uppermost 20 m. According to the available stratigraphy data for the area (Silacheva *et al.*, 2014) these two layers can be, to a first order, assigned to a shallow sand-sandy loam layer and a gravel-sandy-pebbles layer, respectively.

This information has been used to setup the main starting parameters for what will be referred to from now as the summer model. The model with a frozen uppermost one meter layer will be termed the winter model.

Considering the daily temperature measured in Almaty since 1915 (Razuvaev *et al.*, 2008), an average daily value was estimated (Fig. 5). At the time of the 1911 Kemin earthquake, consistent with the available photographs taken a few days after the event that showed snow and ice on the ground (Fig. 2), the air temperature was likely to be well below zero for a few weeks prior to the event. Starting from the average air temperature in Almaty on 3 January, and considering the relationships relating the ground surface temperature to temperature at different depths (Andersland and Ladanyi, 2004) and the evidence regarding the frost penetration in the area of Almaty reported in Teltayev *et al.* (2016), it is reasonable to assume that at least the first meter of soil was frozen at the time of the Kemin earthquake.

Accordingly to Finn *et al.* (1978), who provided shear modulus values as a function of soil temperature, the velocity in the uppermost 1 m layer (considered to be frozen) was fixed to 867 m/s. This value is valid when considering small strains and after having interpolated Finn's curve according to the estimated temperature of the ground using an adjustable

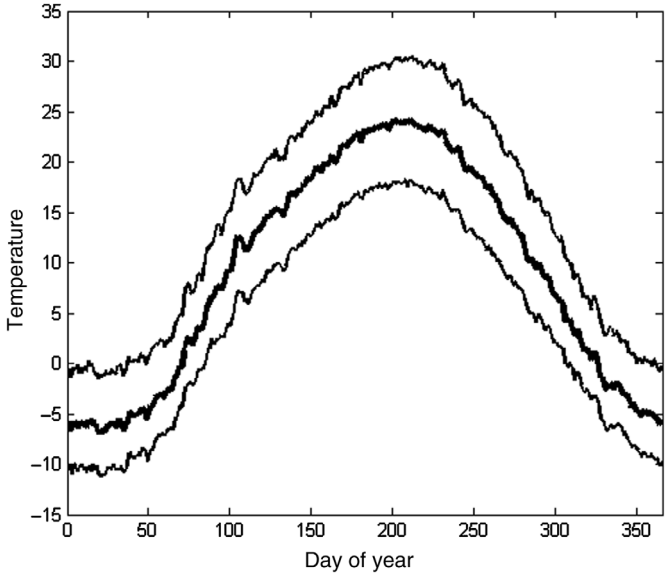

Figure 5. Average daily temperature ± standard deviation of the surface temperature for the city of Almaty. The graph was obtained by averaging the daily temperatures recorded in Almaty between 1915 and 2001.

tension continuous curvature spline. Finally, we tested different positions of the water table depth (1, 3, and 5 m).

Numerical Simulations

To evaluate the role of the frozen surface layer, we carried out the dynamic analyses in terms of effective stress. In this study, the analysis was carried out using the DEEPSOIL software (Hashash *et al.*, 2017), which has the capability to simulate the effect of increasing pore water pressure during earthquake shaking on the dynamic properties of the unfrozen soil, and the drainage and redistribution of pore water pressures under dynamically induced pore pressure gradients.

A time-domain nonlinear analysis was carried out based on solving the equation of motion or dynamic equilibrium equation

$$[M]\{\ddot{u}\} + [C]\{\dot{u}\} + [K]\{u\} = -[M]\{I\}\ddot{u}_g, \tag{1}$$

in which $[M]$ is the mass matrix, $[C]$ is the viscous damping matrix, $[K]$ is the stiffness matrix, is the vector of relative acceleration, $\{\dot{u}\}$ is the vector of relative velocities, $\{u\}$ is the vector of relative displacements, $[\ddot{u}]$ is the acceleration at the base of the soil column, $\{I\}$ is the unit vector, and the $[M]$, [C], and $[K]$ matrices are assembled using the incremental response of the soil layers (Hashash *et al.*, 2010). The soil response is obtained from a constitutive model that describes the cyclic behavior of the soil. Equation (1) is solved numerically at each time step using a time integration method (e.g., the Newmark, 1959, β method).

The soil column is discretized into individual layers using a multi-degree-of-freedom lumped parameter model or finite elements (Kramer, 1996). The calculation process for a nonlinear model is as follows. First, an input acceleration time series is used to determine the motion at the base of the soil profile. Then, the motion at each layer boundary is calculated, moving from the bottom of the soil profile to the top.

The stiffness and damping values for each layer were derived based on the Darendeli (2001) models for sand and gravel deposits, respectively. For the frozen sandy layer at the surface (winter model), the Singh and Donovan (1977) relationships were considered.

The Darendeli (2001) relationships require five input parameters: plasticity index (PI), over consolidation ratio (OCR), mean effective confining pressure (in atmospheres (σ_m'), loading frequency (f) in hertz, and the number of loading cycles (N)). In general, a major role is played by the PI and mean effective confining pressure. To account for the approximate knowledge of the stratigraphy, the analysis considered three values of the PI (PI = 0, 5, 10). However, considering the similarity of the curves for the selected three values, and of the obtained results, only the results of the calculations for PI = 0 (nonplastic soils) will be presented in the following.

Darendeli (2001) found that $G/G_{\max}$ (in which $G_{\max}$ is the shear modulus at zero strain and G is the secant shear modulus), increases slightly for cohesive soils, whereas the ratio does not increase for cohesionless soils, with the OCR. Therefore, we neglected in this study the effect of the OCR. Regarding the surficial frozen layer in the winter model, we adopted the Vinson *et al.* (1977) parameters for typically frozen soils in interior Alaska.

The adopted procedure, implemented in DEEPSOIL, allows the change in pore water pressure and soil degradation due to cyclic loading to be predicted. This includes the strain-based pore pressure generation model of Matasović and Vucetic (1993) for sands, based on the model developed by Dobry *et al.* (1985) for saturated sands. Dobry *et al.* (1985) showed that the residual excess pore pressure ratio, r_u, is proportional to the number of applied shearing cycles N and the increase in shear strain γ. This result was formalized by Vucetic and Dobry (1988) as follows:

$$r_u = \frac{u_N}{\sigma_v'} = \frac{p \times f \times F \times N \times (\gamma - \gamma_{tv})^s}{1 + f \times F \times N \times (\gamma - \gamma_{tv})^s}, \tag{2}$$

in which r_u is the residual excess pore pressure ratio, u_N is the residual excess pore pressure after N cycles, σ_v' is the initial vertical effective stress before shearing, γ_{tv} is the volumetric threshold shear strain, and f, p, F, and k are curve-fitting parameters.

Some empirical correlation relations for the curve-fitting parameters F and s proposed by Carlton (2014) for sands, having the following functional form, have been used:

TABLE 1
Typical Values of Vertical Permeability and the Consolidation Coefficient (Pestana *et al.*, 1997; Carlton, 2014) Considered in This Study

Soil Typical Names	Fine Content Percent (%)	Vertical Permeability (m/s)	Consolidation Coefficient
Clayey sands, sand-silt mixtures or silty sands, sands silt mixtures	12 < FC < 50	3×10^{-5}	0.0612
Poorly graded sand with clay	5 < FC < 12	8×10^{-5}	0.1632
Poorly graded sands or well-graded sand	FC < 5	5×10^{-4}	1.02
Gravels	FC = 0	5×10^{-2}	10.2

FC, percentage of fine content.

$$F = 3810 V_S^{-1.55}, \tag{3}$$

$$s = (\mathrm{FC} + 1)^{0.1252}, \tag{4}$$

in which V_S is the shear-wave velocity in m/s and FC is the percentage of fines content.

DEEPSOIL models the dissipation and redistribution of residual excess pore pressures using the Terzaghi 1D consolidation theory (Hashash *et al.*, 2017), expressed as

$$\frac{\partial u}{\partial t} = C_V \left(\frac{\partial^2 u}{\partial z^2} \right), \tag{5}$$

in which u is the residual excess pore pressure, t is the time, z is the depth, and C_V is the coefficient of consolidation coefficient given by the following formula for the cohesionless soils (sand and gravel) (Carlton 2014):

$$C_V = \frac{k}{m_v \times \gamma_m}, \tag{6}$$

in which C_V is in m^2/s, k is the vertical permeability in m/s, m_v is the volumetric compressibility in m^2/kN, and γ_m is the water unit weight equal to 9.8 kN/m^3.

Based on the Unified Soil Classification System and Pestana *et al.* (1997), both the value of vertical permeability k and the volumetric compressibility m_v were chosen according to their fine material content, as listed in Table 1.

Because of the approximations made with regards to the granulometry of the soil, the numerical simulations have been carried out for different values of FC in the uppermost 10 m of the sand layer. The values are nonetheless considered to be reasonable based on the knowledge of the grain size composition of soils in the study area (Nisii, 2009).

To carry out the numerical simulations, the choice of the input strong-motion time series is crucial. To be able to carry out these simulations as realistically as possible, because no strong-motion recordings of large events in the study area are available (and, obviously, for the studied earthquakes), a selection has to be done considering the available strong-motion data bases. The selection mainly considered recordings for earthquakes with focal mechanisms similar to that estimated for the Kemin (Kulikova and Krüger, 2015) and Verny events, with comparable positions with respect to the fault.

After having searched the international data bases, the input motion was selected from recordings of the 1999 M_w 7.6 Chi-Chi earthquake. This event had a reverse focal mechanism and a hypocentral depth estimated at 21.2 km (Global Centroid Moment Tensor catalog, see Ekström *et al.*, 2012). This depth is similar to that calculated by Mosca *et al.* (2019) and Kulikova and Krüger (2015) for the Kemin and Verny earthquakes. The selected recording was that of station HWA014, which is at a similar location with respect to the epicenter as the city of Verny was with respect to the ruptures that generated the Verny and Kemin earthquakes.

V_{S30}, that is, the travel-time averaged S-wave velocity in the uppermost 30 m, at the selected recording site is equal to 277 m/s, which is slightly different from that estimated in Almaty (245 m/s) from the array measurements. The strong-motion record has been scaled using the SeismoMatch software (Seismosoft, 2016) to account for the differences in magnitude, epicentral distance, and V_{S30}. The software, developed by Abrahamson (1992) and then updated by Hancock *et al.* (2006), modifies an acceleration time history in the time domain to match it with a specified spectrum using the technique proposed by Lilhanand and Tseng (1987, 1988). The target spectrum was generated using the OpenSHA software developed by the Southern California Earthquake Center and the U. S. Geological Survey (Field *et al.*, 2003). A target spectrum was calculated to simulate the Kemin and Verny earthquake recordings by considering the GMPE of Boore and Atkinson (2008), which is recommended by GEM for active shallow crust conditions, such as those at hand.

Table 2 summarizes the main characteristics of the selected and the matched recordings. A PGA value of nearly 0.2g is expected, based on the GMPEs of Boore and Atkinson (2008), to have affect Verny during the considered earthquakes.

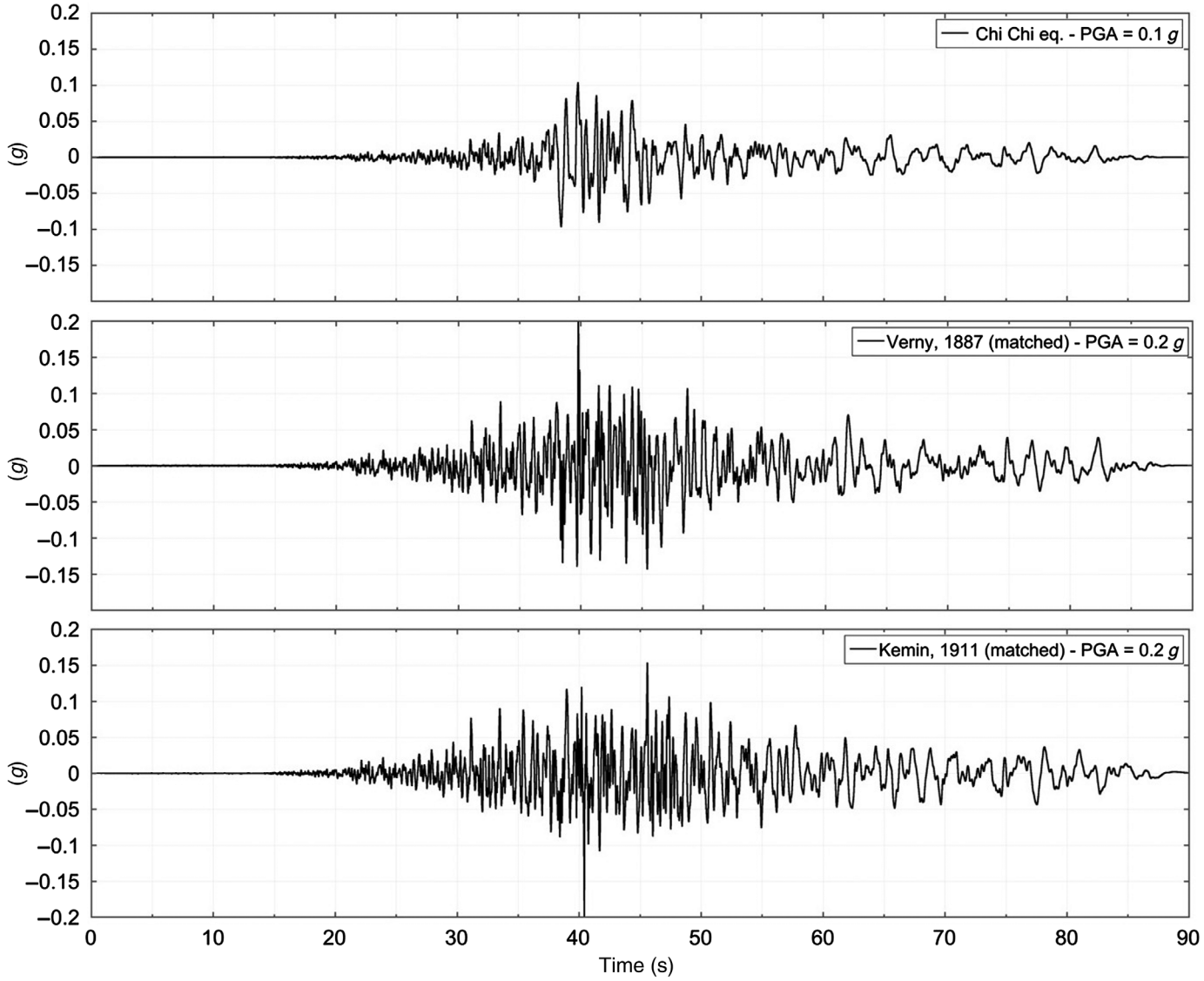

Figure 6. Time series of the 1999 Chi-Chi earthquake (top panel) selected to represent the ground motion experienced in Verny during the Kemin and Verny events. The results of the spectral matching are shown in the central panel for the 1887 Verny earthquake and in the bottom panel for the 1911 Kemin earthquake.

It is worth noting that the recording has been matched with both the Verny and Kemin earthquakes by considering in both cases summer and winter velocity profiles. However, because the analysis carried out showed that the results are not dependent on the employed input recordings, but only on the soil velocity profile, only the results obtained for the Kemin event, with winter soil conditions, and the Verny one, for the summer velocity profile, are shown for sake of brevity. Figure 6 shows the original

TABLE 2
Main Characteristics of the Selected and the Matched Recordings

Event	M_w	*T*	PGA (*g*)	*R* (km)	V_{S30} (m/s)
1999 Chi-Chi earthquake recording (station HWA014)	7.6	Reverse	0.1	52	277
1911 matched Kemin earthquake recording	7.8	Reverse	0.199	40	245
1887 matched Verny earthquake recording	7.3	Reverse	0.202	23	245

M_w, moment magnitude; PGA, peak ground acceleration; *R*, epicentral distance; *T*, rupture type.

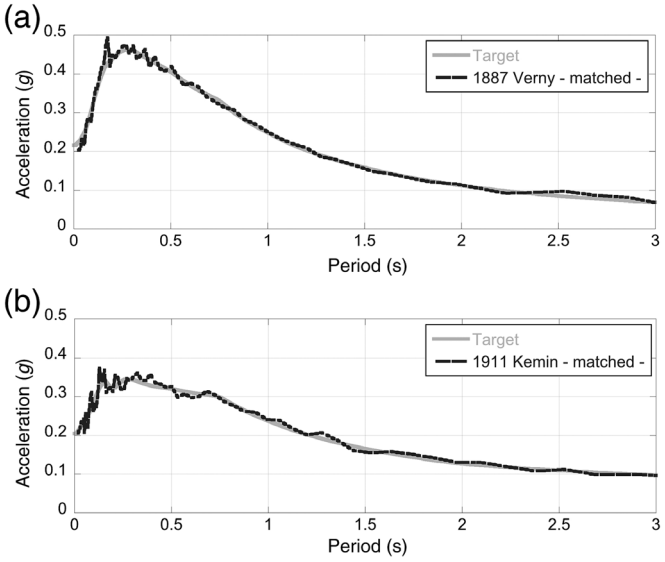

Figure 7. (a) Target and matched response spectrum for the 1887 Verny earthquake (distance 23 km). (b) Target and matched response spectrum for the 1911 Kemin earthquake (distance 40 km).

selected recording and the simulated recordings for the Verny and Kemin earthquake after spectral matching.

The adequacy of the spectral matching procedure is also shown in Figure 7, in which the target response spectra determined by considering the GMPE of Boore and Atkinson (2008) and the matched one are reported.

Results

The results regarding the pore water pressure generation, obtained for site response analysis for the Verny and Kemin earthquakes, are shown in Figure 8, which shows the results as a function of different water table positions (1, 3, and 5 m) and vertical permeability k.

The pore water pressure curves are shown for the maximum values reached during the numerical calculations versus the effective vertical stress curves. It is remarkable that for the two highest k values, the pore water pressure reaches the value of the effective stress at the bottom of the frozen layer.

These k values are also reasonably consistent, although on the lower bound, with the thresholds determined by Finn *et al.* (1978), who found that when k is larger than 10^{-3} m/s, the redistribution of pore water pressure-induced liquefaction in the tested model. On the contrary, when k was smaller than 10^{-4} m/s, no liquefaction occurred.

In all the other cases, drainage through the soil layers up to the surface is allowed, affecting the internal redistribution of pore water pressure. The increases of pore water pressure at around 8 m depth in all of the presented model could be due to the change in the velocity profile at 10 m depth, where an impedance contrast and change in permeability exists between the sand and the gravel layers.

In the following, considering that the results seem to be independent of the chosen position of the water table, only those regarding the water table positioned at 1 m depth will be shown.

Figure 9 shows the pore water pressure at different times during the strong shaking as a function of depth. During the maximum level of shaking, the pore water pressure is increased mainly at 8 m depth, but it reaches a maximum at nearly 8 m and 1 m depth after 60 s (Fig. 9). For the Kemin event, as shown in Figure 9, the pore water pressure at 1 m depth reaches the effective pressure, therefore generating liquefaction. At the end of the strong shaking phase (around 90 s), the pore water pressure has lowered with depth, although for the Kemin event it is still as high as the effective one.

Figure 10 shows the development of the pore water pressure ratio (PWPR) versus time under undrained conditions (Kemin earthquake) and drained conditions (corresponding to those of the Verny earthquake) at a depth of 1 m for the three considered vertical permeability values. Clearly, the PWPR increases with the arrival of the strong ground motion phase (nearly 40 s). For undrained conditions, when k is equal to 5×10^{-4} and 8×10^{-5} m/s, the PWPR reaches a value of 1 after 55 and 80 s, respectively. This is obviously due to the larger values of k facilitating the migration of pore water pressure to the soil in a shorter time. When k is equal to 3×10^{-5} m/s, the PWPR increases steadily, but remains at values as low as 20% at the end of the strong ground shaking.

Under drained conditions, the two lower k values lead to a continuous increase of the PWPR, starting after the strong-motion phase arrival. When the highest value of the vertical permeability is considered, a decrease of the PWPR is observed after 60 s. From Figures 8–10, it is therefore clear that the frozen layer inhibits the drainage to the surface and allows the pore water pressure to reach the value of the effective stress, therefore increasing the liquefaction potential.

Discussion and Conclusions

In this study, we attempted to provide an explanation for the different well-documented coseismic effects (mainly ground failure and liquefaction) of two historical earthquakes that occurred in Central Asia, namely the 1887 M_w 7.3 Verny and the 1911 M_w 7.8 Kemin earthquakes. Considering the scarcity of available geotechnical data, we developed different models of the subsurface structure and considered different positions of the water table. After having selected a suitable recording of the ground motion to match what is believed to have been the situation during these events, and adequately scaled it by means of a spectral matching procedure, we carried out dynamic analysis. The results indicated that, for values of vertical permeability compatible with the soil typology of the study area, the presence of a shallow frozen layer whose presence is likely in winter considering the available knowledge of

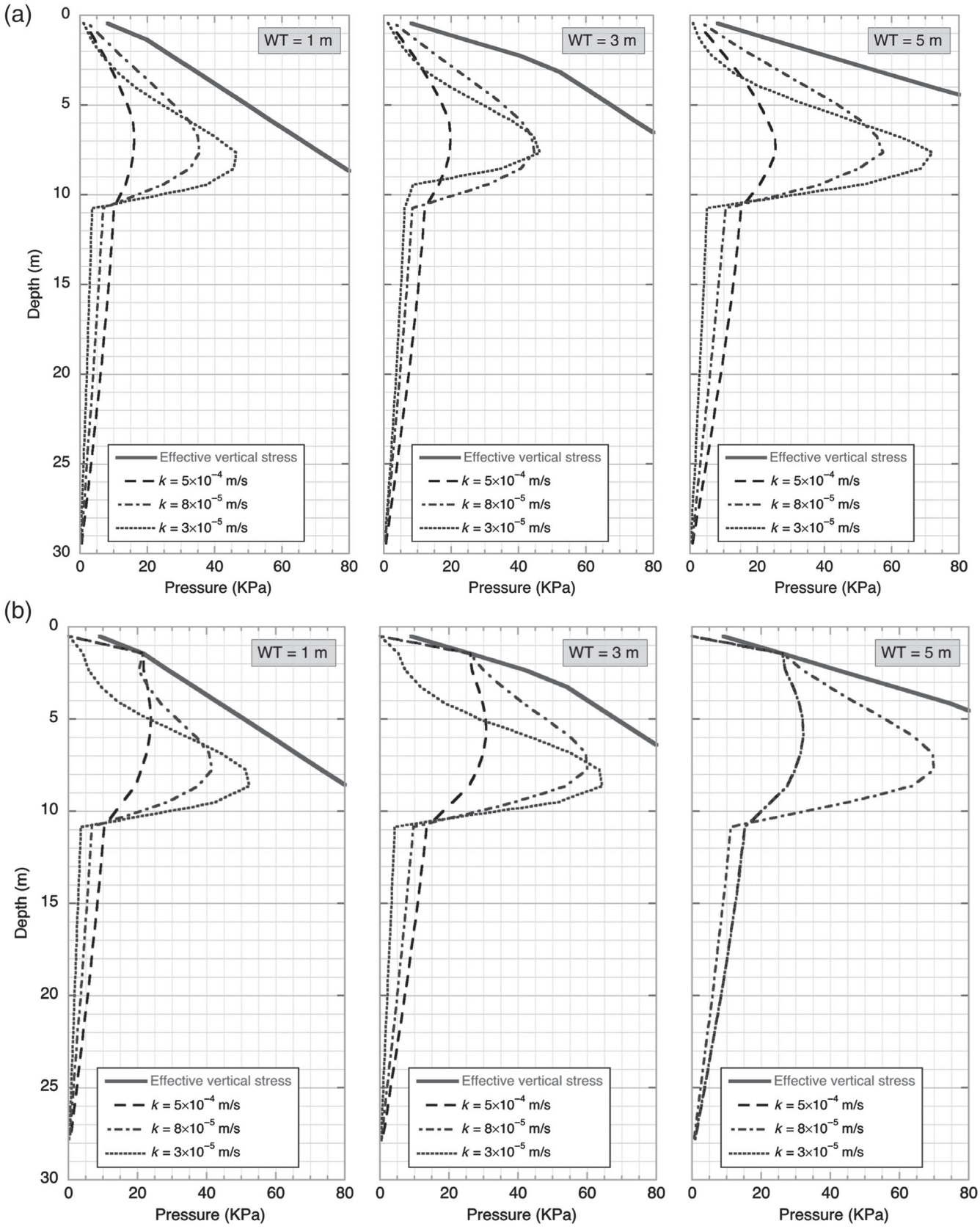

Figure 8. Maximum pore water pressure versus depth while considering different water table (WT) depths (from left to right, 1, 3, and 5 m, respectively). Different line styles (dashed, dotted–dashed–continuous) show the results obtained for three different values of vertical permeabilities (k). The thick black line indicates the effective vertical stress. (a) Results obtained for the summer profile and the Verny event. (b) Results obtained for the winter profile and the Kemin event.

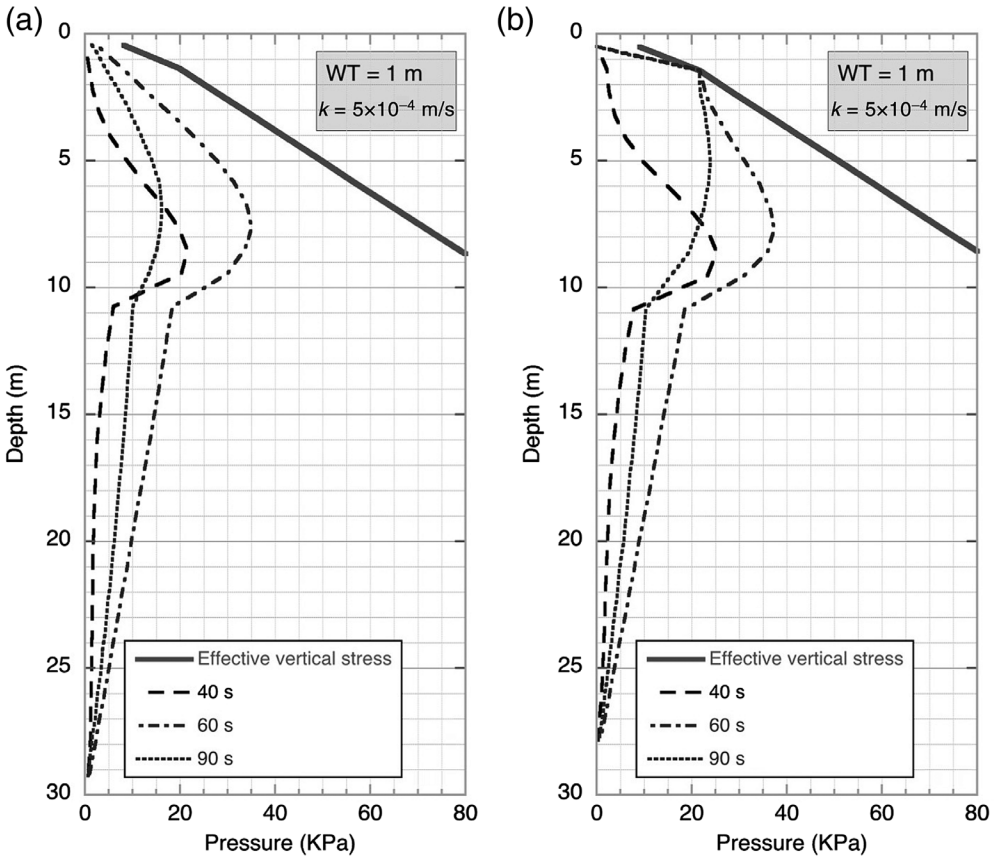

Figure 9. Pore water pressure versus depth at different time for the case of the water table at 1 m depth (see Fig. 6 for the reference time). The dashed line shows the pore water pressure distribution with depth after 40 s, the dashed–dotted line shows after 60 s, and the dotted line shows after 90 s. The thick black line depicts the effective vertical stress. (a) Results for the Verny earthquake. (b) Results for the Kemin earthquake. WT, water table.

soil conditions and the air temperature in the area, could have increased the liquefaction potential of shallow layers by preventing the external drainage of pore water pressure. This could have in turn lead the large amount of ground failure observed during the 3 January 1911 Kemin earthquake.

In fact, an internal redistribution of pore water pressure could have occurred because of the seismically induced pore water pressure gradient. As a result, the pore water pressure ratio could have increased in the uppermost layers of the unfrozen soils where the effective stress is low. We showed that the higher the vertical permeability, the faster the transfer of seismically induced pressures and the higher the susceptibility of the unfrozen saturated layer to liquefaction in the upper levels.

We are aware that our study is based on a still poor data set. Nevertheless, we think that, because the parameters used in this work are scientifically sound for the material existing in the area, and the level of ground motion considered was reasonable for the size and epicentral of the considered event, the obtained results shed some light on the importance of secondary effects that could affect the city during earthquake shaking.

Furthermore, these results highlight the importance, in areas where due to cold winter the shallow most soil layer is frozen, of assessing the effect of local soil amplification on ground motion and considering the seasonal influence on secondary effects such as liquefaction and ground failure.

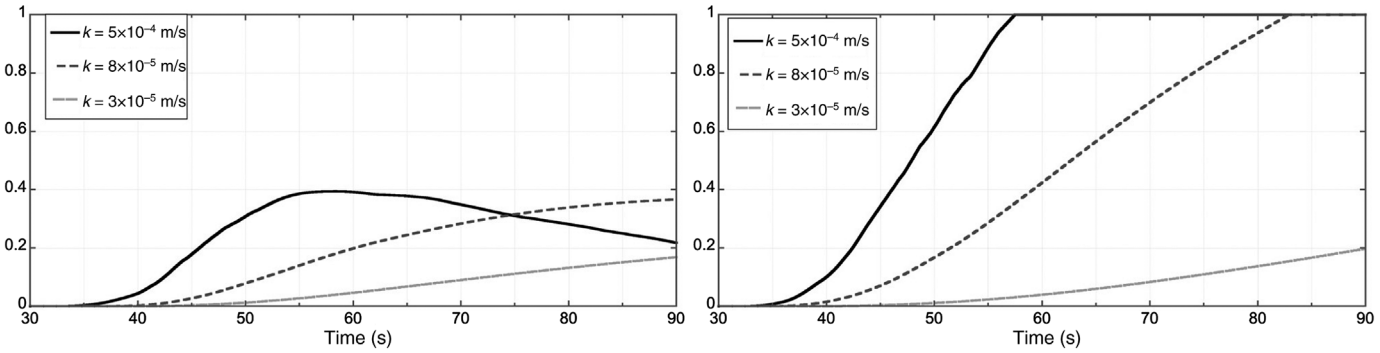

Figure 10. Pore water pressure development at a depth of 1 m, considering the depth of the water table being equal to 1 m for different values of k.

We also remark that a careful analysis of the available description of the effects of an historical earthquake, while qualitative, could still provide important hints for quantitative analyses and an improvement of a quantitative assessment of seismic hazard and risk.

Data and Resources

All data used in this article came from published sources listed in the references. Some plots were made using the Generic Mapping Tools version 5.4.5 (www.soest.hawaii.edu/gmt; Wessel and Smith, 1998, last accessed June 2019). The Earthquake Model Central Asia (EMCA) project is available at http://www.emca-gem.org (last accessed June 2019).

Acknowledgments

This research was made possible, thanks to the support of the International Center for Theoretical Physics (Trieste, Italy). The authors thank D. Bindi and S. Orunbaev for the help in the field work. M. Santulin provided suggestions for the spectral matching procedure. K. Fleming kindly improved our English.

References

Abrahamson, N. A. (1992). Non-stationary spectral matching, *Seismol. Res. Lett.* **63,** 30.

Andersland, O. B., and B. Ladanyi (2004). *Frozen Ground Engineering*, John Wiley & Sons, Hoboken, New Jersey, 384 pp.

Arrowsmith, J. R., C. J. Crosby, A. M. Korzhenkov, E. Mamyrov, I. Povolotskaya, B. Guralnik, and A. Landgraf (2017). Surface rupture of the 1911 Kebin (Chon–Kemin) earthquake, Northern Tien Shan, Kyrgyzstan, *Geol. Soc. Lond. Spec. Publ.* **432,** 233–253.

Bindi, D., S. Parolai, A. Gómez-Capera, M. Locati, Z. Kalmetyeva, and N. Mikhailova (2014). Locations and magnitudes of earthquakes in Central Asia from seismic intensity data, *J. Seismol.* **18,** 1–21.

Bogdanovic, K. I. (1911). An earthquake of December 22, 1910 (January 4, 1911) in northern chains of the Tien Shan between Verny and Issyk-Kul, *Proc. Geol. Comm.* **30,** 329–419.

Bogdanovich, K. I., I. M. Kark, B. Y. Korolkov, and I. V. Muchketov (1914). Earthquake of the 4th January 1911 in the northern districts of the Tien Shan, *Trans. Geol. Comm. Ser.* **89,** 270.

Boore, D., and G. Atkinson (2008). Ground-motion prediction equations for the average horizontal component of PGA, PGV, and 5%-damped PSA at spectral periods between 0.01 s and 10.0 s, *Earthq. Spectra* **24,** 99–138.

Carlton, B. (2014). An improved description of the seismic response of sites with high plasticity soils, organic clays, and deep soft soil deposits, *Ph.D. Thesis*, University of California, Berkeley.

Darendeli, M. B. (2001). Development of a new family of normalized modulus reduction and material damping curves, *Ph.D. Dissertation*, University of Texas at Austin, Austin, Texas.

Dobry, R., A. Vasquez-Herrera, R. Mohamad, and M. Vucetic (1985). Liquefaction flow failure of silty sand by torsional cyclic tests, in *Advances in the Art of Testing Soils Under Cyclic Conditions*, V. Khosla (Editor), American Society of Civil Engineers, New York, New York, 29–50.

Ekström, G., M. Nettles, and A. M. Dziewonski (2012). The global CMT project 2004-2010: Centroid-moment tensors for 13,017 earthquakes, *Phys. Earth Planet. In.* **200/201,** 1–9, doi: 10.1016/j.pepi.2012.04.002.

Field, E. H., T. H. Jordan, and C. A. Cornell (2003). OpenSHA: A developing community-modeling environment for seismic hazard analysis, *Seismol. Res. Lett.* **74,** 406–419.

Finn, L., R. N. Yong, and K. W. Lee (1978). Liquefaction of thawed layers in frozen soils, *J. Geotech. Eng. Div. ASCE* **104,** 1243–1255.

Hancock, J., J. Watson–Lamprey, N. A. Abrahamson, J. J. Bommer, A. Markatis, E. M. M. A. McCoy, and R. Mendis (2006). An improved method of matching response spectra of recorded earthquake ground motion using wavelets, *J. Earthq. Eng.* **10,** 67–89.

Hashash, Y. M. A., M. I. Musgrove, J. A. Harmon, O. Ilhan, D. R. Groholski, C. A. Phillips, and D. Park (2017). *DEEPSOIL 7.0, User Manual*, Board of Trustees of University of Illinois at Urbana-Champaign, Urbana, Illinois.

Hashash, Y. M. A., C. Phillips, and D. R. Groholski (2010). Recent advances in non-linear site response analysis, *International Conferences on Recent Advances in Geotechnical Earthquake Engineering and Soil Dynamics*, 8, available at http://scholarsmine.mst.edu/icrageesd/05icrageesd/session12/8 (last accessed June 2019).

Kramer, S. L. (1996). *Geotechnical Earthquake Engineering*, Prentice Hall, Upper Saddle River, New Jersey, 653 pp.

Krüger, F., G. Kulikova, and A. Landgraf (2017). Instrumental magnitude constraints for the 11 July 1889, Chilik earthquake, *Geol. Soc. Lond. Spec. Publ.* **432,** 41–72.

Kulikova, G., and F. Krüger (2015). Source process of the 1911 M 8.0 Chon-Kemin earthquake: Investigation results by analogue seismic records, *Geophys. J. Int.* **201,** 1891–1911.

Lilhanand, K., and W. S. Tseng (1987). Generation of synthetic time histories compatible with multiple damping design response spectra, *SMiRT-9*, Lausanne, Switzerland, K2/10, 105–110.

Lilhanand, K., and W. S. Tseng (1988). Development and application of realistic earthquake time histories compatible with multiple damping design spectra, *Proc. of the 9th WCEE*, Vol. II, Tokyo–Kyoto, Japan, 819–824.

Matasović, N., and M. Vucetic (1993). Cyclic characterization of liquefiable sands, *J. Geotech. Eng.* **119,** 1805–1822.

Mosca, I., B. Baptie, S. Sargeant, and R. T. Walker (2019). Integrating outcomes from probabilistic and deterministic seismic hazard analysis in the Tien Shan, *Bull. Seismol. Soc. Am.* **109,** 688–715.

Newmark, N. M. (1959). A method of computation for structural dynamics, *J. Eng. Mech. Div.* **85,** 67–94.

Nisii, O. (2009). Study on risk management of earthquakes in the city of Almaty, Republic of Kazakhstan, *Final Report*, Japan International Cooperation Agency, OYO International Corp., Nippon Koei Co., Ltd., Tokyo, Japan, 134 pp.

Nurmagambetov, A., N. Mikhailova, and W. Iwan (1999). Seismic hazard of the Central Asia region, in *Seismic Hazard and Building Vulnerability in Post-Soviet Central Asian Republics*, S. A. King, V. I. Khalturinand, and B. E. Tucker (Editors), Kluwer Academic Publishers, Dordrecht, The Netherlands, 1–43.

Ohori, M., A. Nobata, and K. Wakamatsu (2002). A comparison of ESAC and FK methods of estimating phase velocity using arbitrarily shaped microtremor arrays, *Bull. Seismol. Soc. Am.* **92,** 2323–2332.

Parolai, S., M. Picozzi, S. M. Richwalski, and C. Milkereit (2005). Joint inversion of phase velocity dispersion and H/V ratio curves from

seismic noise recordings using a genetic algorithm, considering higher modes, *Geophys. Res. Lett.* **32,** 1–4.

Pestana, J. M., C. E. Hunt, and R. R. Goughnour (1997). *FEQDrain: A Finite Element Computer Program for the Analysis of the Earthquake Generation and Dissipation of Pore Water Pressure in Layered Sand Deposits with Vertical Drains*, Report No. UCB/EERC-97-15, Earthquake Engineering Research Center, University of California, Berkeley, California.

Pilz, M., T. Abakanov, K. Abdrakhmatov, D. Bindi, T. Boxberger, B. Moldobekov, S. Orunbaev, N. Silacheva, S. Ullah, S. Usupaev, *et al.* (2015). An overview on the seismic microzonation and site effect studies in central Asia, *Ann. Geophys.* **58,** no. 1, S0104, doi: 10.4401/ag-6662.

Razuvaev, V. N., E. G. Apasova, and R. A. Martuganov (2008). Daily temperature and precipitation data for 223 former-USSR stations, *ORNL/CDIAC-56, NDP-040*, Carbon Dioxide Information Analysis Center, Oak Ridge National Laboratory, U.S. Department of Energy, Oak Ridge, Tennessee, doi: 10.3334/CDIAC/cli.ndp040.

Seismosoft (2016). SeismoMatch v2.1—A computer program for spectrum matching of earthquake records, available at http://www.seismosoft.com (last accessed June 2019).

Silacheva, N., U. Kulbayeva, and N. Kravchenko (2014). Seismic ground motion variations resulting from site conditions, *Geodes. Geodynam.* **5,** 9–15.

Singh, S., and N. C. Donovan (1977). Seismic response of frozen-thawed soil systems, *Proc. of the 6th International Conference on Earthquake Engineering*, New Delhi, India, 10–14 January, paper no. 19, session 6, preprints, 611–616.

Teltayev, B., A. Baibatyrov, and E. Suppes (2016). Characteristics of highway subgrade frost penetration in regions of the Kazakhstan, *Japanese Geotech. Soc. Spec. Publ.* **2,** 1664–1668.

Ullah, S. (2016). Seismic hazard assessment in Central Asia: Combining site effects investigations and probabilistic seismic hazard, *Doctoral Dissertation*, Technische Universität Berlin, Berlin, 163 pp.

Vinson, T. S. (1978). Response of frozen ground to dynamic loadings, in *Geotechnical Engineering for Cold Regions*, O. B. Andersland and D. M. Anderson (Editors), McGraw-Hill Book Co., New York, New York, 405–458.

Vinson, T. S., R. Czajkowski, and J. Li (1977). Dynamic properties of frozen cohesionless soils under cyclic triaxial loading conditions, *Rept. No. MSU-CE-77-1*, Division of Engineering Research, Michigan State University, East Lansing, Michigan.

Vucetic, M., and R. Dobry (1988). Cyclic triaxial strain-controlled testing of liquefiable sands, in *Advanced Triaxial Testing of Soil and Rock*, R. Donaghe, R. Chaney, and M. Silver (Editors), ASTM International, West Conshohocken, Pennsylvania, 475–485, doi: 10.1520/STP29093S.

Wang, L., X. Ling, X. Xu, and Q. Hu (2004). Study on response spectrum characteristics of earthquake acceleration for roadbed on permafrost site, *Chin. J. Rock Mech. Eng.* **23,** 1330–1335.

Wessel, P., and W. H. F. Smith (1998). New, improved version of the Generic Mapping Tools released, *EOS Trans. AGU* **79,** 579.

Xu, G., Z. Yang, U. Dutta, L. Tang, and E. Marx (2011). Seasonally frozen soil effects on the seismic site response, *J. Cold Reg. Eng.* **25,** 53–70.